

# Structure and mechanical properties of naturally occurring lightweight foam-filled cylinder – The peacock's tail coverts shaft and its components



Z.Q. Liu <sup>a,\*</sup>, D. Jiao <sup>a</sup>, M.A. Meyers <sup>b</sup>, Z.F. Zhang <sup>a,\*</sup>

<sup>a</sup> Shenyang National Laboratory for Materials Science, Institute of Metal Research, Chinese Academy of Sciences, Shenyang 110016, China

<sup>b</sup> Department of Mechanical and Aerospace Engineering, Materials Science and Engineering Program, University of California San Diego, La Jolla, CA 92093, USA

## ARTICLE INFO

### Article history:

Received 9 September 2014

Received in revised form 27 November 2014

Accepted 26 January 2015

Available online 4 February 2015

### Keywords:

Biological materials

Feather shaft

Hierarchical structure

Buckling

Mechanical properties

## ABSTRACT

Feather shaft, which is primarily featured by a cylinder filled with foam, possesses a unique combination of mechanical robustness and flexibility with a low density through natural evolution and selection. Here the hierarchical structures of peacock's tail coverts shaft and its components are systematically characterized from millimeter to nanometer length scales. The variations in constituent and geometry along the length are examined. The mechanical properties under both dry and wet conditions are investigated. The deformation and failure behaviors and involved strengthening, stiffening and toughening mechanisms are analyzed qualitatively and quantitatively and correlated to the structures. It is revealed that the properties of feather shaft and its components have been optimized through various structural adaptations. Synergetic strengthening and stiffening effects can be achieved in overall rachis owing to increased failure resistance. This study is expected to aid in deeper understandings on the ingenious structure–property design strategies developed by nature, and accordingly, provide useful inspiration for the development of high-performance synthetic foams and foam-filled materials.

© 2015 Acta Materialia Inc. Published by Elsevier Ltd. All rights reserved.

## 1. Introduction

Lightweight cellular solids or foams and foam-filled structures have attracted great attention owing to their unique properties, such as outstanding kinetic energy absorption efficiency from impacts, high strength-to-density ratio, and good insulation ability [1]. So far, a huge number of synthetic foams and foam-filled materials have been exploited and widely applied in various fields, e.g., buildings, transport systems and biomedical implants. Besides the composition, structure plays a dominant role in determining the properties of cellular materials [1,2]. Accordingly, the structural design and control have invariably been a central focus for property optimization. In this respect, nature has achieved great successes and may serve as a fruitful source of insights and inspiration. There are numerous biological materials with cellular structures in nature, such as wood, bone, porcupine quill, avian beak and feather rachis [1–10]. Through long-period natural evolution and selection, the structures and properties of these materials have been optimized for their particular functions, despite the fact that most of them are synthesized using weak elements at ambient

conditions [9]. For instance, the bending resistance of avian beaks can be improved by three to six times without significantly increasing the density through incorporating closed-cell foam into exterior shell [10]. Owing to the notable properties and plentiful resources, some naturally occurring cellular materials, e.g., wood, have found widespread engineering applications [1,8]. Moreover, valuable inspiration may be generated for exploiting synthetic foams and foam-filled materials by mimicking the ingenious structures [3,5,11], e.g., titanium foams for bone substitutes and porous polymer scaffolds for tissue engineering [12,13]. Therefore, it has broad implications to elucidate the structure and mechanical properties, especially their relationships, in natural biological cellular materials.

As one of the most complex integumentary appendages in vertebrates, feathers possess a hierarchically branched construction based on a central shaft and fused with a series of barbs [14,15]. As the primary mechanical supporter, feather shaft can be divided into two parts along its length. The most proximal section, termed calamus, is anchored into follicle and featured as a hollow tube. In comparison, the majority of shaft, the feather rachis, is manifested by a near cylindrical cortex shell filled with medullary foam. Feathers have evolved to be robust and flexible enough to withstand the aerodynamic forces during flight, yet still maintaining a low density

\* Corresponding authors. Tel.: +86 24 23971043; fax: +86 24 23891320.

E-mail addresses: liuzq@imr.ac.cn (Z.Q. Liu), zhfzhang@imr.ac.cn (Z.F. Zhang).

[14–16]. They also aid in the thermal insulation, waterproofing, camouflage, and even courtship [17]. Owing to these attributes and their potential inspiration, feathers are drawing an increasing attention and research interest [14,15,18–29]. It is reported that feathers are composed of feather keratin which can be classified as the so-called  $\beta$ -keratin made of  $\beta$ -sheets [28–30]. The arrangement of  $\beta$ -sheets at the molecular level has been elucidated through experiments [18–21]. The mechanical properties of feather shaft as well as cortex and foam have also been preliminarily evaluated [22–29]. Nevertheless, a systematic understanding is still far from being achieved on the structures, mechanical properties, deformation and failure behaviors of feather shaft and its components, especially from a viewpoint of materials science. Meanwhile, the mechanical behaviors have rarely been correlated to the structures so far [15]. As a result, it still remains unclear about the involved mechanisms that make feathers strong and tough.

The peacock, or the male peafowl in the pheasant family, is primarily featured by its extravagant tail coverts which are normally used for sexual displaying, frightening predators and fighting with rivals. Though contributing little to flying, the tail coverts do bear substantial stresses from both their own weight and external loads during above processes [28]. Meanwhile, they are long and thick among various avian feathers and thus may provide samples in sufficient size for experiments. In this study, the structures of peacock's tail coverts shaft and its components are systematically characterized. The mechanical properties, deformation and failure behaviors are analyzed. The strengthening, stiffening and toughening mechanisms are investigated.

## 2. Materials and experimental procedures

### 2.1. Materials

Naturally shed tail coverts in length of  $\sim 105$  cm of healthy adult peacocks (*Pavo cristatus*) were purchased from a local farm.

Feather shafts were obtained by cutting off the vanes. The apparent densities of shaft and its components were obtained by dividing their weights using volumes determined by optical observation. The mean moisture content was measured to be  $\sim 7.9$  wt.% through adequately drying the shafts at  $105^\circ\text{C}$  for 5 h. The dried shafts were then ashed at  $560^\circ\text{C}$  for 40 h. The mineral content (or ash content) was quantified as the ratio between weight of ash and that of original dried sample [31].

### 2.2. Structural characterization

Different types of specimens have been adopted for structural analysis. A feather shaft was transversely sectioned using a low speed diamond saw at different positions along its length with intervals of 1 cm near the proximal and 7 cm for the majority of rachis. The proximal part of another shaft was sectioned in the longitudinal direction. These samples were then mounted in epoxy, ground and polished to mirror finish. Fractured shafts were also prepared by manually tearing for examination. The structure was characterized by laser scanning confocal microscopy (LSCM) using an Olympus LEXT OLS 4000 3D-measuring microscope and field emission scanning electron microscopy (SEM) on an LEO Supra 35 instrument. Samples were sputter-coated with a film of gold prior to SEM observation. The surface roughness was measured according to LSCM using the accessory software. At least 90 foam cells from random regions were analyzed for each position to determine the cell sizes. X-ray computed micro-tomography (XCT) was employed to visualize the three-dimensional morphologies of foam by an Xradia-Versa XRM 500 scanner with a voxel size of  $0.68 \mu\text{m}$ . The phase constituents of both cortex and ash of shaft were examined by X-ray diffraction (XRD) using a D/MAX-2500PC diffractometer. The ash was further characterized by transmission electron microscopy (TEM) using an FEI Tecnai G2 F20 system.

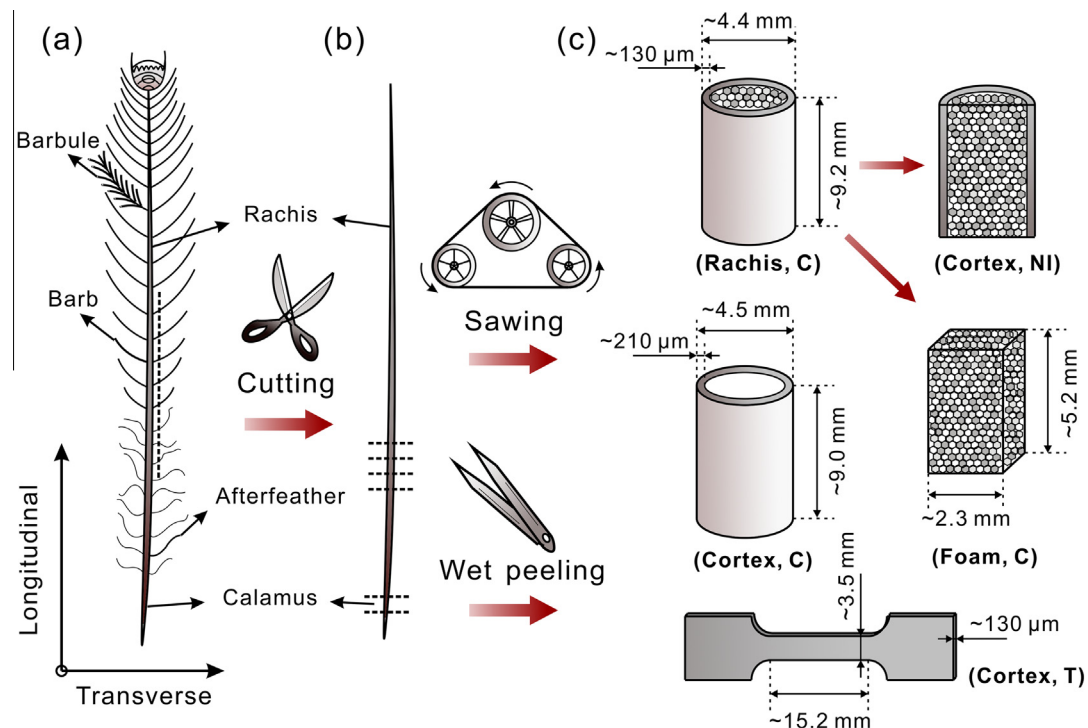


**Fig. 1.** Schematic illustrations for preparation procedures of the mechanical testing samples and their nominal dimensions. NI, C and T represent the testing methods of nanoindentation, compression and tension, respectively.

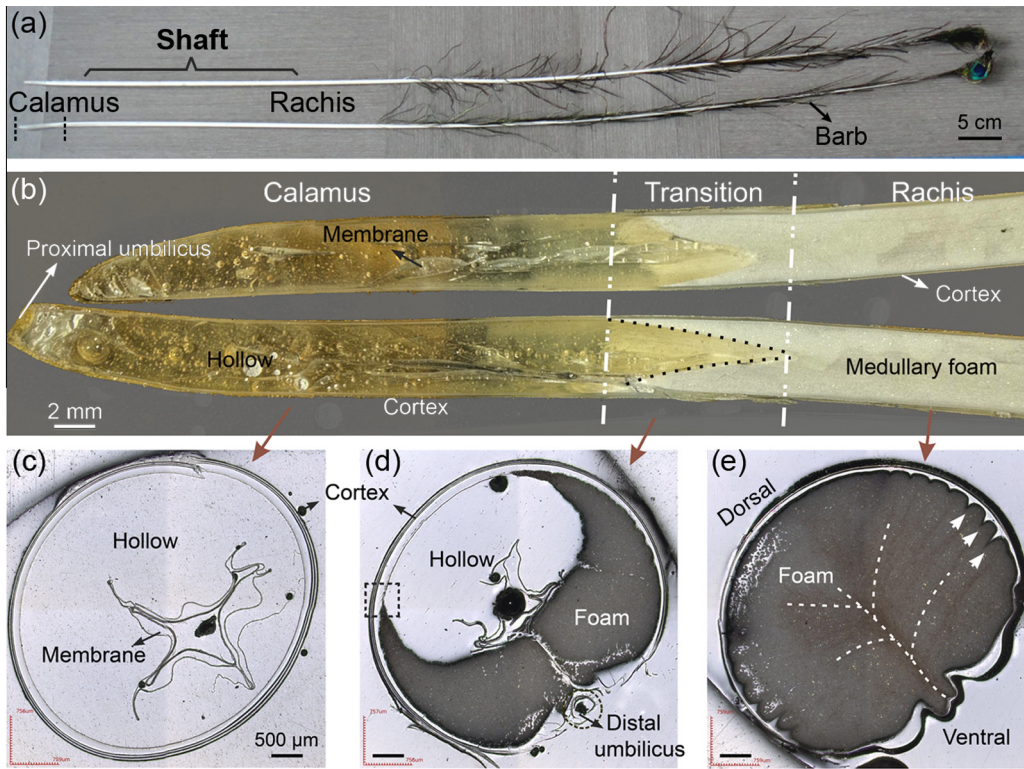


**Fig. 2.** Morphologies of (a) peacock's tail coverts shaft and (b) longitudinal sections of the proximal part. (c)–(e) Representative transverse sections corresponding to calamus, transition region and rachis, respectively. The boundaries of transition region are denoted by dashed lines in (b). The septa and ridges in the rachis are indicated by dashed curves and arrowheads respectively in (e).

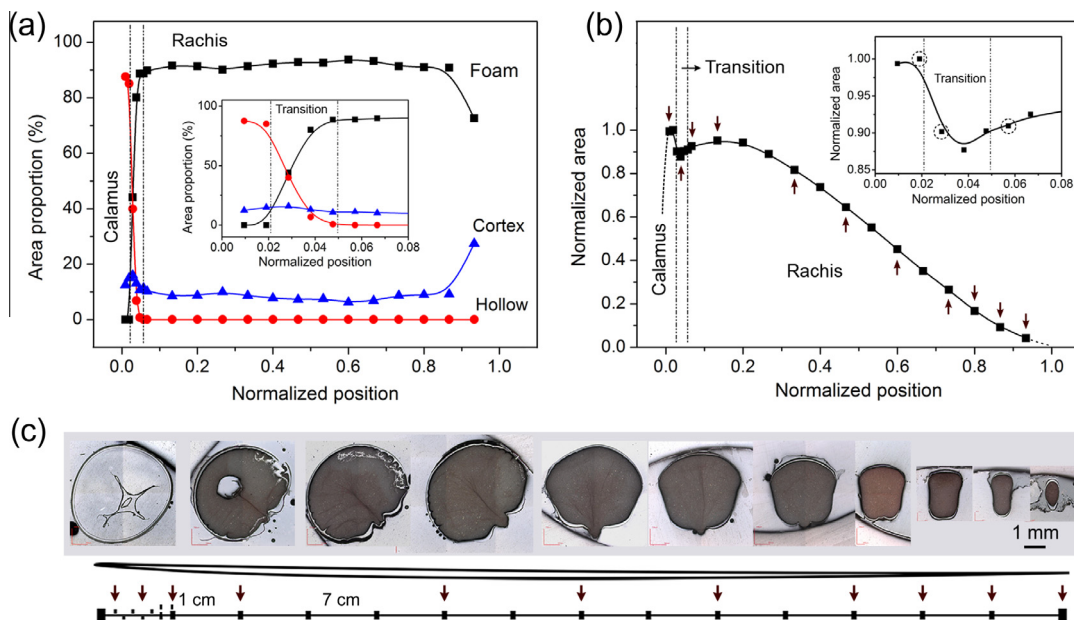


**Fig. 3.** (a) Relative area proportions of cortex, foam and hollow space in the transverse sections and (b) variation in normalized cross-sectional area as a function of normalized position for feather shaft along its length. The transition region is magnified in insets. Typical transverse appearances at different positions as indicated by the arrows are shown in (c). The circled points in inset of (b) denote the positions corresponding to the sections shown in Fig. 2(c)–(e).

### 2.3. Mechanical testing

The preparation procedures of samples for mechanical testing and their nominal dimensions are schematically illustrated in

**Fig. 1.** Cylindrical rachis and hollow cortex for compression were excised from the middle region and calamus of shaft, respectively, using a low speed diamond saw. Rectangular compressive samples of medullary foam were obtained from the rachis by cutting off

**Table 1** Density, mineral content and mechanical properties of cortex, foam and overall feather rachis. C and T represent compression and tension, respectively. The ultimate strength and failure strain denote the critical stress and strain corresponding to the onset of stress drop or plateau for materials without instantaneous failure, i.e. foam and wet cortex and rachis.

	Density (g/cm <sup>3</sup> )	Mineral content (wt%)	Stress state	Sample condition	Young's modulus (GPa)	Specific Young's modulus (kNm/g)	Ultimate strength (MPa)	Specific strength (N/m/g)	Failure strain (%)
Cortex	0.811 ± 0.008	0.343 ± 0.006	C	Dry	4.13 ± 0.09	5.1 ± 0.1	92.4 ± 2.9	114 ± 4	2.8 ± 0.3
				Wet	2.38 ± 0.04	—	38.9 ± 2.3	—	2.4 ± 0.2
Foam	0.037 ± 0.001	0.446 ± 0.007	T	Dry	3.1 ± 0.4	3.8 ± 0.5	203.3 ± 17.5	250 ± 20	14.7 ± 2.0
				Wet	1.9 ± 0.1	—	99.5 ± 7.6	—	17.4 ± 1.9
Rachis	0.133 ± 0.001	—	C	Dry	0.017 ± 0.004	0.47 ± 0.08	0.55 ± 0.03	14.7 ± 0.7	4.7 ± 0.8
				Wet	0.0053 ± 0.0005	—	0.148 ± 0.007	—	3.8 ± 0.3
	0.133 ± 0.001	—	C	Dry	0.62 ± 0.01	4.68 ± 0.09	13.8 ± 0.6	104 ± 5	2.5 ± 0.2
				Wet	0.32 ± 0.02	—	4.9 ± 0.3	—	1.8 ± 0.1

exterior cortex. For preparing the tensile specimens of cortex, the rachis was firstly soaked in water to improve its flexibility. Then the cortex was carefully peeled from rachis and cut into dog-bone shape. Dry samples were dried in air for at least 5 days and wet samples were obtained by soaking in water for one day before testing. The accurate dimensions of all samples were measured by optical microscopy. The geometric and structural changes in the longitudinal direction can be neglected for these samples within their length scales owing to the considerable length of shaft.

Uniaxial compression and tension tests were performed at a constant strain rate of  $1 \times 10^{-3} \text{ s}^{-1}$  at room temperature under a relative humidity of ~30%. The wet samples were continuously irrigated with water during testing. At least four samples were measured for each test. The macroscopic compressive deformation process of foam was monitored using a Keyence VW9000 high speed microscope. Variations in the hardness and Young's modulus of cortex throughout its thickness were evaluated by nanoindentation on the polished longitudinal section. This was conducted at a displacement-control mode with a constant indentation speed of 10 nm/s and depth of 1.5 μm. 15 data points were measured for each position at the same thickness. The deformation and failure morphologies were examined by SEM after coating samples with gold.

### 3. Structures of feather shaft and its components

#### 3.1. Constituent and geometry

[Fig. 2\(a\)](#) shows the macroscopic appearance of peacock's tail coverts. The longitudinal sections of the proximal part are magnified in [Fig. 2\(b\)](#). A transition region exists between the calamus and rachis, i.e., locating near skin, of which the boundaries are denoted by dashed lines. Representative transverse cross sections of the calamus, transition region and rachis are displayed in [Fig. 2\(c\)–\(e\)](#), respectively. The interior of calamus is almost hollow except that a membranous core extends from the proximal umbilicus to the foam at the center. In the transition region, increasing medullary foam arises preferentially from the ventral side along cortex. In comparison, the rachis is fully filled with foam. The proportions of cortex, foam and hollow space, manifested by their relative area ratios, in the shaft as a function of the normalized position along its length are presented in [Fig. 3\(a\)](#). It is seen that, despite the distinct variations at the most proximal and distal parts, the constituent remains almost constant with ~90% foam and ~10% cortex in rachis.

The feather shaft also manifests different geometric characters along its length. As shown in [Fig. 3\(b\)](#), the cross-sectional area decreases almost monotonically toward the distal end for most part. In particular, a notable necking occurs in the transition region, as magnified in the inset, which may be caused by the clamping of skin muscle. This is expected to help to prevent the easy shedding of feathers. Typical transverse morphologies at different positions are presented in [Fig. 3\(c\)](#). The outer appearance continuously transforms from a circular ring at the calamus to a symmetrical fan-like shape at the main rachis. Then, the section gradually becomes near rectangular beyond ~65% of total length and elliptical at the tip. Meanwhile, the distribution of components across the shaft, though symmetrical, appears quite non-uniform. The cortex is invariably thicker on the dorsal and ventral sides compared with the lateral edges.

It has been revealed that the constituent and geometry are important factors controlling the mechanical response of shaft to aerodynamic forces in flying feathers [22,23,32,33]. For the

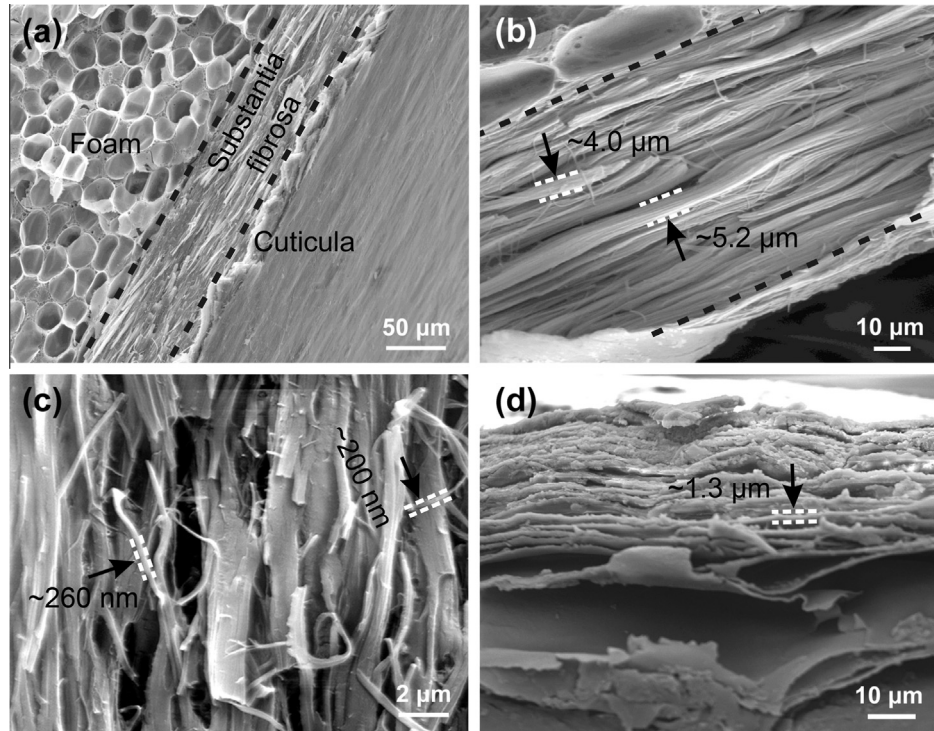


**Fig. 4.** SEM micrographs of the cortex in feather shaft.

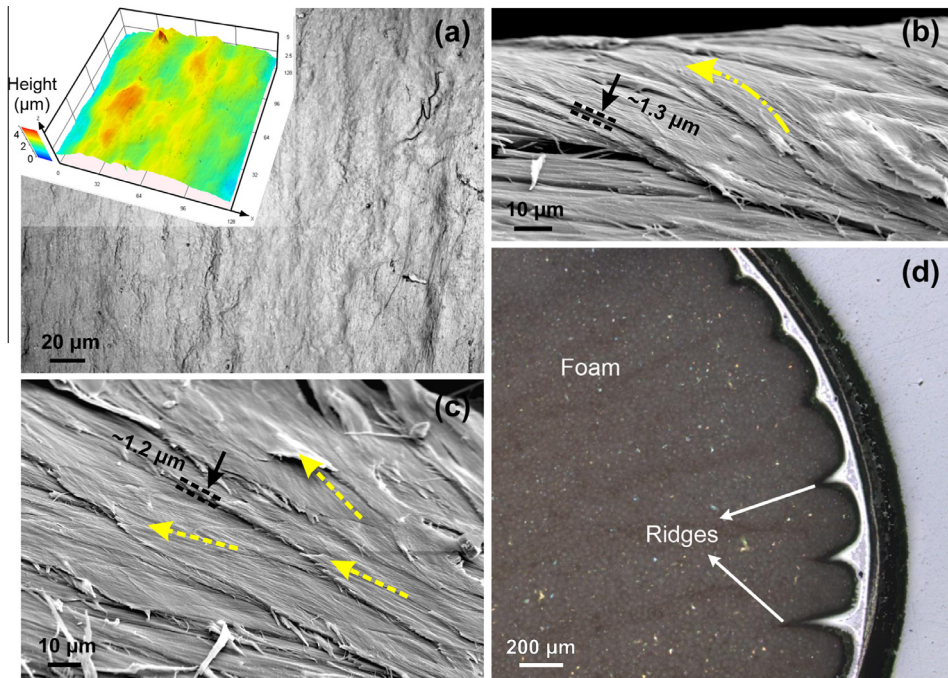


**Fig. 5.** (a) Top view and (b, c) morphologies of the cuticula layer in cortex and (d) ridges at the interface between foam and cortex. LSCM three-dimensional surface morphology of cortex is shown in the inset in (a).

present peacock's tail coverts, bending, especially along the dorsal–ventral direction, acts as the dominant loading mode [28]. The resistance to bending is primarily manifested by the flexural stiffness which scales with Young's modulus and the second moment of area [22,33]. From a weight minimization perspective, the whole cross-sectional area decreases gradually along the length with the

decrease in bending moment. Nevertheless, the bending resistance may not be severely deteriorated as a consequence. On the one hand, the vertical elongation of shape favors a higher second moment of area in the bending direction. On the other hand, the resistance also benefits from the unique distribution of components because the apparent modulus of cortex is much higher than

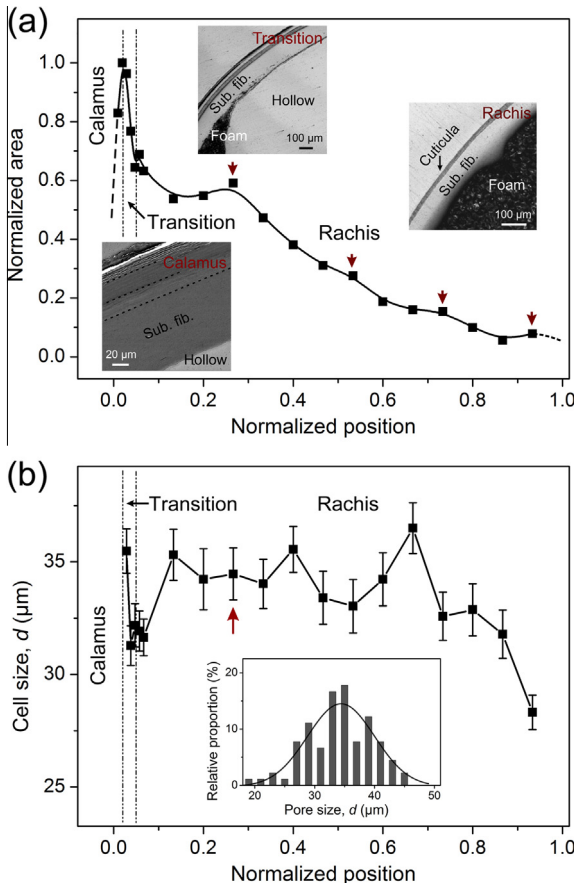


**Fig. 6.** Variations in the (a) normalized cross-sectional area of cortex and (b) cell size of foam as a function of normalized position along the length. Representative transverse morphologies of cortex for calamus, transition region and rachis are shown in the insets in (a). The inset in (b) presents the representative cell size distribution of foam at the position denoted by arrow.

that of foam (Table 1). In such a scenario, sufficient flexural stiffness can be achieved in feather shaft through the above adaptations, giving rise to a high mechanical efficiency [16].

### 3.2. Cortex

It is reported that the cortex can be divided into two layers throughout its thickness, i.e., the inner substantia fibrosa adjacent to foam and the outer cuticula [22,33]. As shown in Fig. 4, in the present feather shaft, the substantia fibrosa is composed of fiber bundles in diameters of  $\sim 3\text{--}6 \mu\text{m}$  highly oriented along the length. The individual fibers, which are also arranged in the same direction, have a diameter of  $\sim 200\text{--}300 \text{ nm}$ . The bundles are further organized in a series of parallel lamellae circumferentially surrounding the foam (Fig. 4(d)). Analogously, the cuticula is also constructed by peripherally packed sub-layers with a smaller periodicity of  $\sim 1.2\text{--}1.3 \mu\text{m}$ . The outer surface of cuticula manifests a squamous morphology, as shown in Fig. 5(a). The surface roughness  $R_a$ , i.e., the arithmetic average of surface height, was measured to be  $0.68 \pm 0.05 \mu\text{m}$  (see inset). Besides, the arrangement of fibers is quite different from that in substantia fibrosa. The fibers are tilted by  $\sim 10\text{--}30^\circ$  against each other in neighboring lamellae (Fig. 5(b) and (c)). As a consequence, a staggered meshwork of crossed fibers is formed at the surface of shaft which serves as a corset helically enveloping the inner substance. In addition, a series of arrowhead-shaped ridges extend from the substantia fibrosa into foam at the lateral sides, resulting in a serrated interface between them (Fig. 5(d)). This is

expected to contribute to a tight bonding between the two components by increasing the interfacial area [34].

The variation in the normalized cross-sectional area of cortex along the length and typical transverse morphologies corresponding to the calamus, transition region and rachis are shown in Fig. 6(a). The area decreases monotonically toward the distal end except for the abrupt increase at calamus. Some discontinuities exist at certain positions with intervals of  $\sim 20\text{--}30 \text{ cm}$ , as denoted by the arrowheads. This may be associated with the varying growth rate of tail coverts caused by fluctuations in living and nutrition conditions [28]. Moreover, the constituent of cortex manifests slight difference between calamus and rachis. The calamus is wrapped by two additional layers which become thinner along the length and peel off at the root rachis.

### 3.3. Medullary foam

It has been revealed that the medullary foam is constituted by closed cells in avian feathers [14,26]. Fig. 6(b) shows the variation in the equivalent diameter of foam cells along the length for the present feather shaft. The cells have relatively large sizes while emergence and then manifest an apparent shrinkage. The cell sizes remain around  $\sim 35 \mu\text{m}$  at the rachis and exhibit a sharp decrease approaching the distal end. As displayed in Fig. 7(a), the medullary foam has an extremely low density that its pieces can be placed on a dandelion and even its individual pappus without causing obvious deflection of them. Branched septa extend from the center of ventral side toward the dorsal and lateral edges, forming emitting stiffeners, as denoted by the dashed curves in Fig. 7(b). The cells are polyhedral or even spherical in shape and the membranes are extremely thin to be nearly transparent under SEM (Fig. 7(c)). The foam struts, having thickness less than  $\sim 5 \mu\text{m}$ , are interconnected in the three-dimensional space to form a continuous skeleton (Fig. 7(d)). This may serve as the primary load supporter to increase the mechanical stiffness and stability of foam.

Further examinations reveal that the foam cells adjacent to cortex are distinctly elongated in the longitudinal direction, leading to a smooth transition between them, as shown in Fig. 8(a). Whereas the struts and membranes are more closely packed in the septa, there is still certain amount of hollow space within them (Fig. 8(b)). In addition, the struts *per se* contain abundant pores of smaller sizes (Fig. 8(c)), resulting in a hierarchically cellular structure of foam. Furthermore, the membranes are weaved by randomly oriented fibers in diameters of  $\sim 200\text{--}300 \text{ nm}$  (Fig. 8(d)), which are similar to those of fibers in cortex. Occasionally, some of membranes may not be fully sealed, yielding some leaks on them.

### 3.4. Hierarchical structure overview

Although both cortex and foam are constructed by  $\beta$ -keratin fibers [28–30], the arrangements of fibers are markedly different between the two components. Also, the mineral content of foam was measured to be slightly higher than that of cortex, as listed in Table 1. As shown in Fig. 9, the mineral can be identified as hydroxyapatite ( $\text{Ca}_5(\text{PO}_4)_3\text{OH}$ ) crystals according to the X-ray and electron diffraction results of the ash [35,36]. The mineral platelets appear in near round shape with diameters of  $\sim 40\text{--}100 \text{ nm}$ , as manifested by the TEM micrographs. To our best knowledge, this is the first direct observation of the mineral in feathers. Furthermore, the present results have been incorporated with the fine structure of  $\beta$ -keratin fibers reported in the literature to give a systematic understanding on the hierarchical structure of feather rachis. It has been revealed that the  $\beta$ -keratin fibers are assembled with parallelly oriented bundles of fibrils at the nanometer scale [20,21,37]. According to the convincing model proposed by Fraser et al. based on experimental results [19,20], the fibril is composed

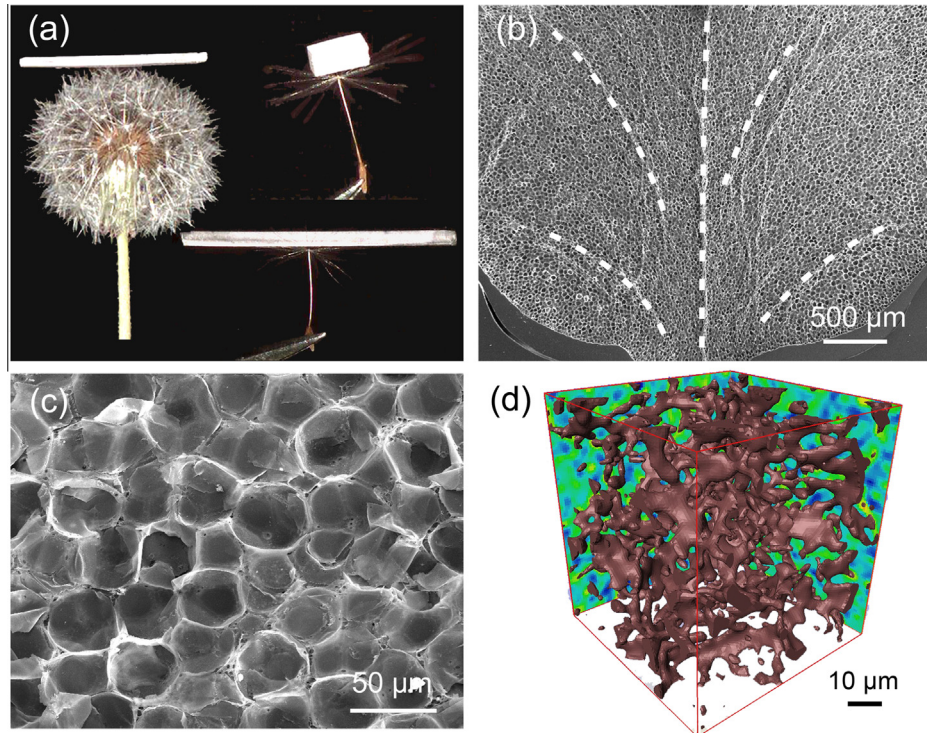


**Fig. 7.** (a) Foam pieces placed on a dandelion and its individual pappus as well as (b, c) SEM and (d) reconstructed three-dimensional XCT micrographs of the foam. The dashed curves in (b) denote the septa.

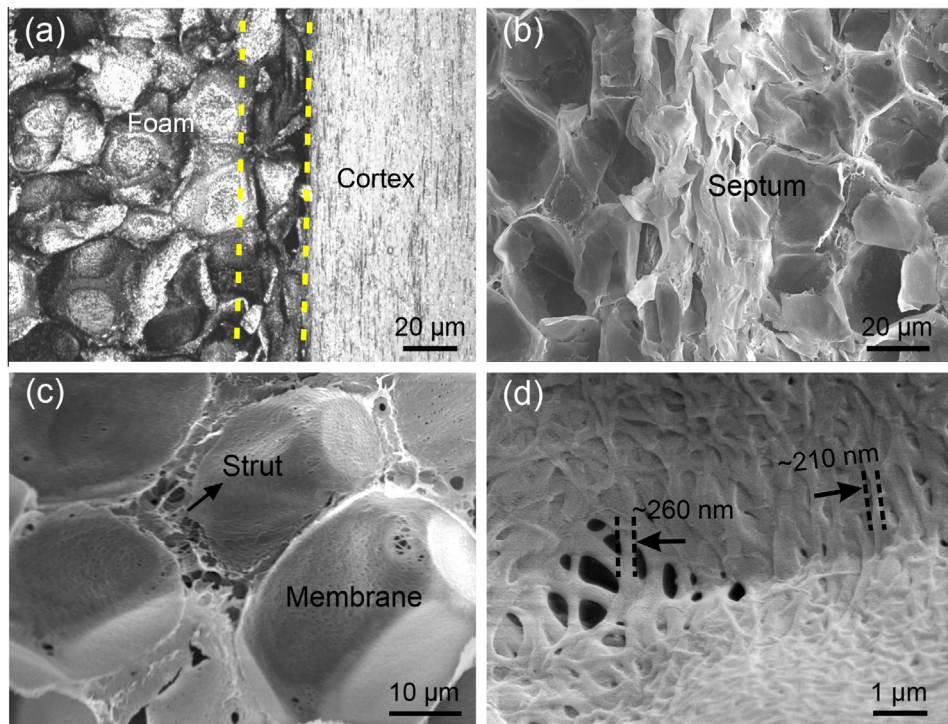


**Fig. 8.** Fine morphologies of (a) the interface between foam and cortex as well as the (b) septum, (c) strut and (d) membrane in foam.

of two twisted  $\beta$ -sheets in diameter of  $\sim 3.3$  nm arranged in a helical mode with a periodicity of  $\sim 9.5$  nm. Each pitch consists of four blocks twisted by  $90^\circ$  against each other. Because only about one third of known amino acids have been identified as forming the  $\beta$ -keratin crystallites, a matrix possibly in amorphous state has been envisaged fusing the fibrils [20,37]. Meanwhile, at a larger

length scale, it has been verified that the fibers are embedded in an amorphous keratinous matrix [14]. The amorphous structure of matrix can also be corroborated by the broad diffraction hump of cortex (Fig. 9(a)). The hierarchical structure, in particular the type and size of constituents, at multiple length scales are schematically illustrated in Fig. 10.

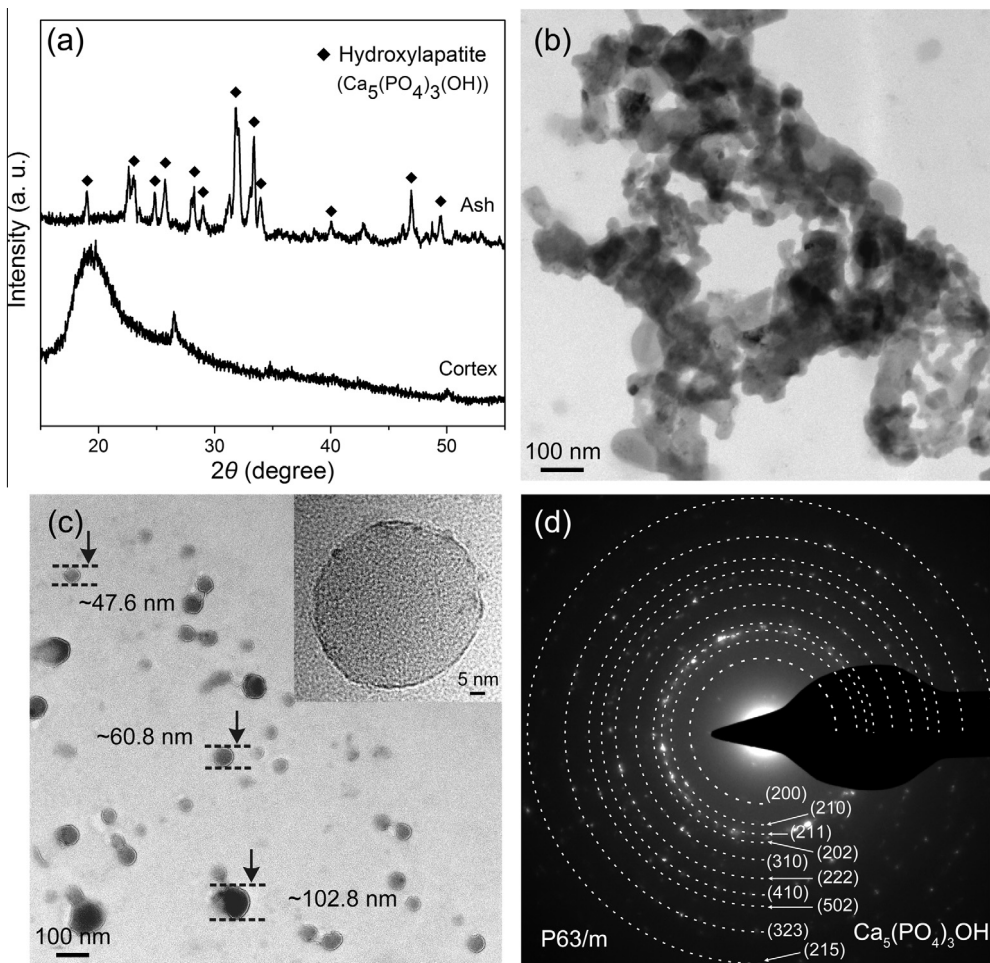


**Fig. 9.** (a) XRD patterns of the cortex and ash of feather shaft as well as (b, c) TEM micrographs and (d) electron diffraction pattern of the mineral platelets in ash. The magnified view of one individual platelet is shown in the inset in (c).

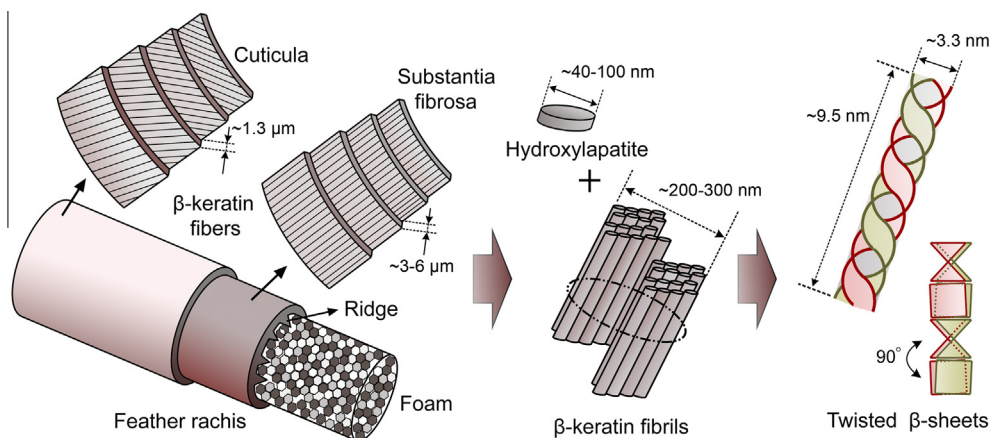


**Fig. 10.** Schematic illustration of the hierarchical structure of feather rachis at different length scales.

#### 4. Mechanical properties, failure behaviors and mechanisms

##### 4.1. Cortex

The variations in the hardness and Young's modulus measured by nanoindentation along the thickness of cortex are presented in Fig. 11. Poisson's ratio is assumed to be 0.3 which is commonly

used for biological materials [2,4,6,10]. Both hardness and Young's modulus exhibit some fluctuations and an apparent decrease at the center of substantia fibrosa. Fig. 12 shows representative compressive and tensile stress-strain curves of the cortex under dry and wet conditions with macroscopic appearances of failed samples in insets. Corresponding mechanical properties are listed in Table 1. Under compression, the dry cortex exhibits negligible plasticity

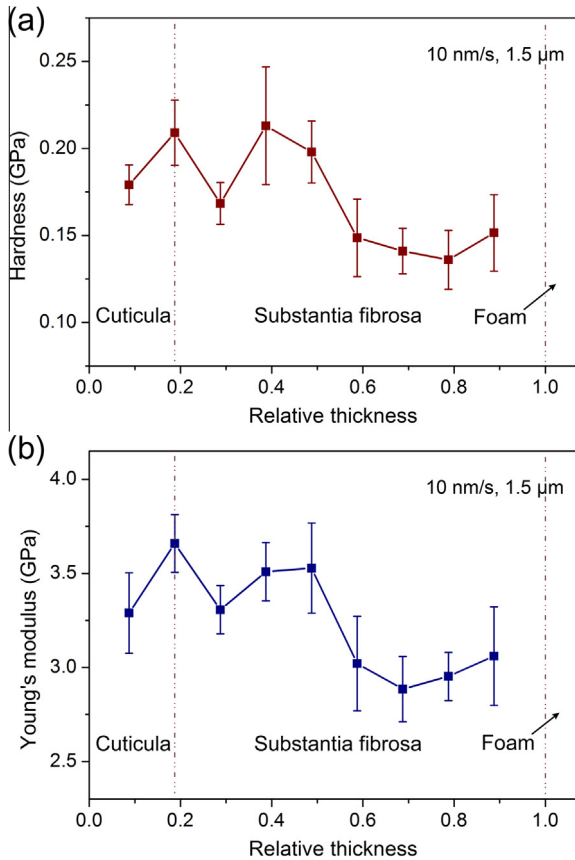


**Fig. 11.** Variations in the (a) hardness and (b) Young's modulus measured by nanoindentation throughout the thickness of cortex.

and/or viscoelasticity and fails at an ultimate strength of  $\sim 92.4$  MPa with a strain of  $\sim 0.028$ . The sample splits into several pieces at the end. Nevertheless, the stress-strain curve of wet cortex is featured by a sharp drop at  $\sim 38.9$  MPa and a subsequent stress plateau around 15 MPa. The sample deforms in the non-axisymmetric diamond buckling mode (inset) [38,39]. The stress increases steeply after  $\sim 75\%$  strain when the buckled wrinkles are compacted. In comparison, the dry cortex exhibits an apparent strain hardening behavior till final fracture under tension. The ultimate strength and failure strain are up to about 2 and 5 times higher than those under compression, respectively. For the wet sample, the failure strain is further increased and a nominal plastic stage is pronounced. Yet the strength and Young's modulus are decreased concomitantly.

The notable compression-tension mechanical asymmetry is tightly associated with the distinct deformation and failure mechanisms. In general, the moisture level of natural avian feathers is typically lower than 10 wt.% [40,41], which conforms to the case of present dry samples. Indeed, feathers can play a waterproofing effect for birds [5,28]. Thus the cases for dry samples have been mainly focused in this study. Under compression, macroscopic axial splitting and subsequent buckling of separated pieces tend to occur at the end of cortex, as shown in Fig. 13(a). The splitting extends in the longitudinal direction and creates a zig-zag fracture morphology throughout the thickness (Fig. 13(b)). The crack is bridged by several lamellae or fiber bundles oriented at different angles with respect to the axis, which hinders the easy crack opening and propagation. The fracture and pulling out of bridges may also help to consume more energy. Meanwhile, both delamination and intralamellar rupture can be observed for the cuticula layer,

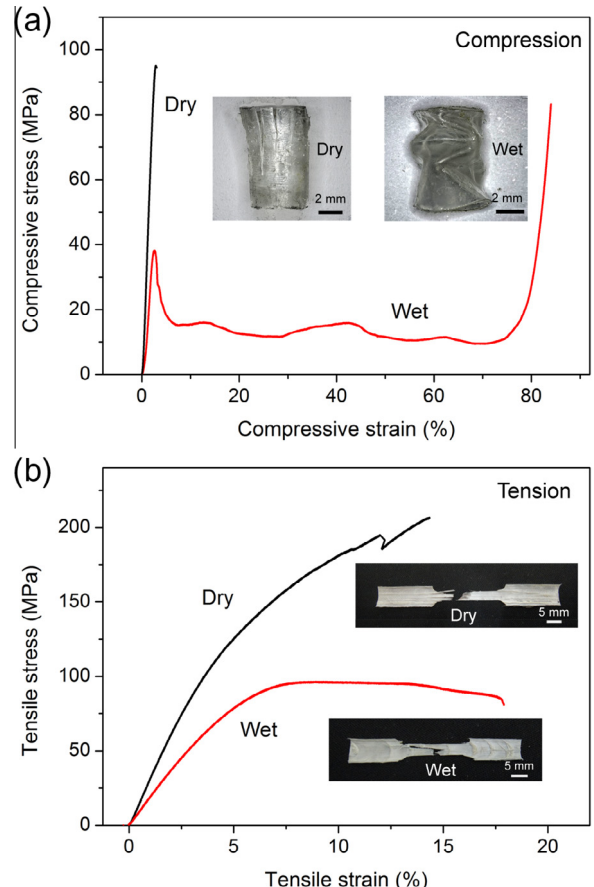


**Fig. 12.** Typical (a) compressive and (b) tensile stress-strain curves for cortex under dry and wet conditions. Macroscopic morphologies of failed samples are shown in insets.

especially in the buckled region (Fig. 13(c)). The outer lamellae are severely wrinkled and locally buckled, and some parts of them are even peeled off from the surface, as shown in Fig. 13(d). Furthermore, the delamination can be suppressed by the intersection between lamellae oriented in different directions (Fig. 13(e)). Besides, the intralamellar microcracks can be bridged by abundant fibers and fiber bundles (Fig. 13(f)). These mechanisms also contribute to a higher resistance to the failure of cortex.

In comparison, the substantia fibrosa and cuticula are detached from each other under tension, as shown in Fig. 14(a). Whereas the final fracture occurs across the transverse plane, the substantia fibrosa has undergone severe axial splitting in the longitudinal direction, resulting in a rather tortuous crack path. The fibers are stretched to rupture and pulled out along the tensile axis (Fig. 14(b)). The splitting planes are bridged by sharing fibers and fiber bundles which may be heavily distorted as a result of sliding between them (Fig. 14(c)). On the opposite side, the cuticula also fractures along a wavy path (Fig. 14(d)). Abundant microcracks are formed in the longitudinal direction and bridged by uncracked ligaments. In analogous to the case under compression, the outer surface demonstrates characteristic morphologies of intra- and interlamellar debonding, both of which are retarded by the inclined overlapping of lamellae, as shown in Fig. 14(e). Besides, some of fibers and fiber bundles are peeled off due to the sliding between adjacent sub-layers on the inner surface (Fig. 14(f)). Therefore, the failure of cortex under compression and tension is intrinsically dominated by the separation and rupture of fibers, respectively. This gives rise to the significant differences in strength and failure strain.

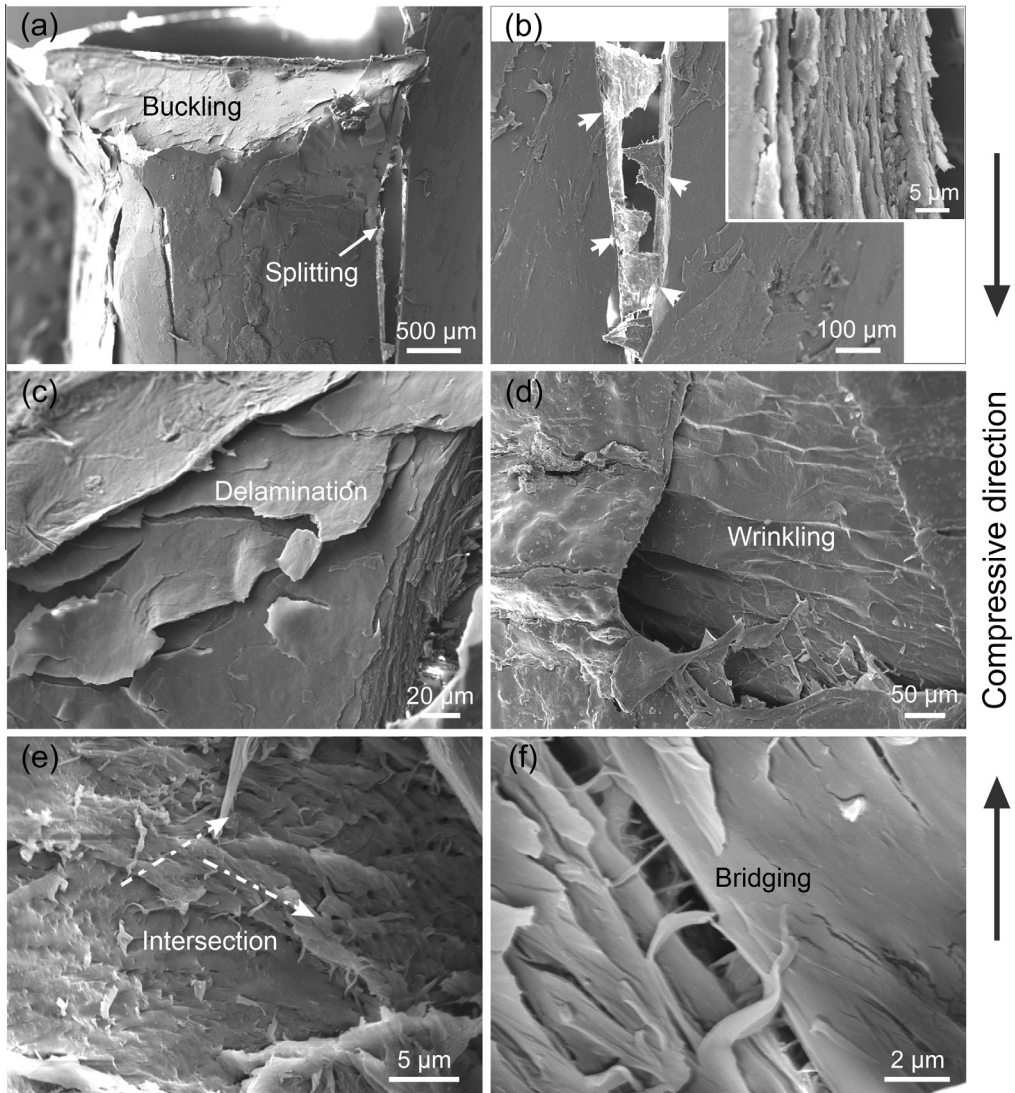


**Fig. 13.** SEM micrographs of dry cortex shell after compressive failure.

Because both splitting and buckling processes are involved in the compressive failure of cortex, it is necessary to determine their relative sequence and to distinguish the dominant strength-controlling mode. According to the theory of elastic stability [38,39], buckling occurs for a thin-walled hollow cylinder with radius  $a$  and wall thickness  $t$  at a critical stress of

$$\sigma_b^c = \frac{Et}{a\sqrt{3(1-\nu^2)}}, \quad (1)$$

where  $E$  and  $\nu$  denote Young's modulus and Poisson's ratio, respectively. By treating the transverse section as a uniform ring, the equivalent values of  $a$  and  $t$  for the cortex can be estimated as 2.326 and 0.127 mm, respectively, according to optical observations. Accordingly, the theoretical buckling strength can be calculated as  $\sim 136.5$  MPa, which is much higher than the measured ultimate strength of  $\sim 92.4$  MPa. Therefore, splitting or intralamellar separation of fiber bundles must occur prior to buckling, dominating the strength of cortex. This is also corroborated by the experimental results that buckling can only be observed in the split pieces rather than the whole cortex.

#### 4.2. Medullary foam

As shown in Fig. 15(a), the compressive stress-strain curves of medullary foam under both dry and wet conditions can be divided into three stages typical for cellular materials, i.e., linear elasticity, stress plateau and densification. At the stress plateau, the sample continuously deforms accompanied by the progressive collapse of foam cells and reduction in porosity [1,2]. Both the plateau stress and Young's modulus are more than 3 times higher for the dry sample compared with the wet one. Representative lateral appearances of the dry foam at different strains are displayed in Fig. 15(b). Macroscopic buckling initiates from the center of sample and develops toward the ends till the onset of final densification at a strain of  $\sim 0.75$ . This results in significant intrusion and protrusion on the opposite sides. An average energy absorption efficiency of  $\sim 13$  J/g per unit weight or  $480$  kJ/m<sup>3</sup> per unit volume is achieved before densification. Moreover, most of strain can be recovered in certain period of relaxation after unloading even though the foam has been compacted by  $\sim 90\%$  (insets). This indicates that a high component of viscoelasticity is involved in overall deformation.

Fig. 16 shows the morphologies of partially recovered dry foam after compression. The lateral surface is featured by a staggered

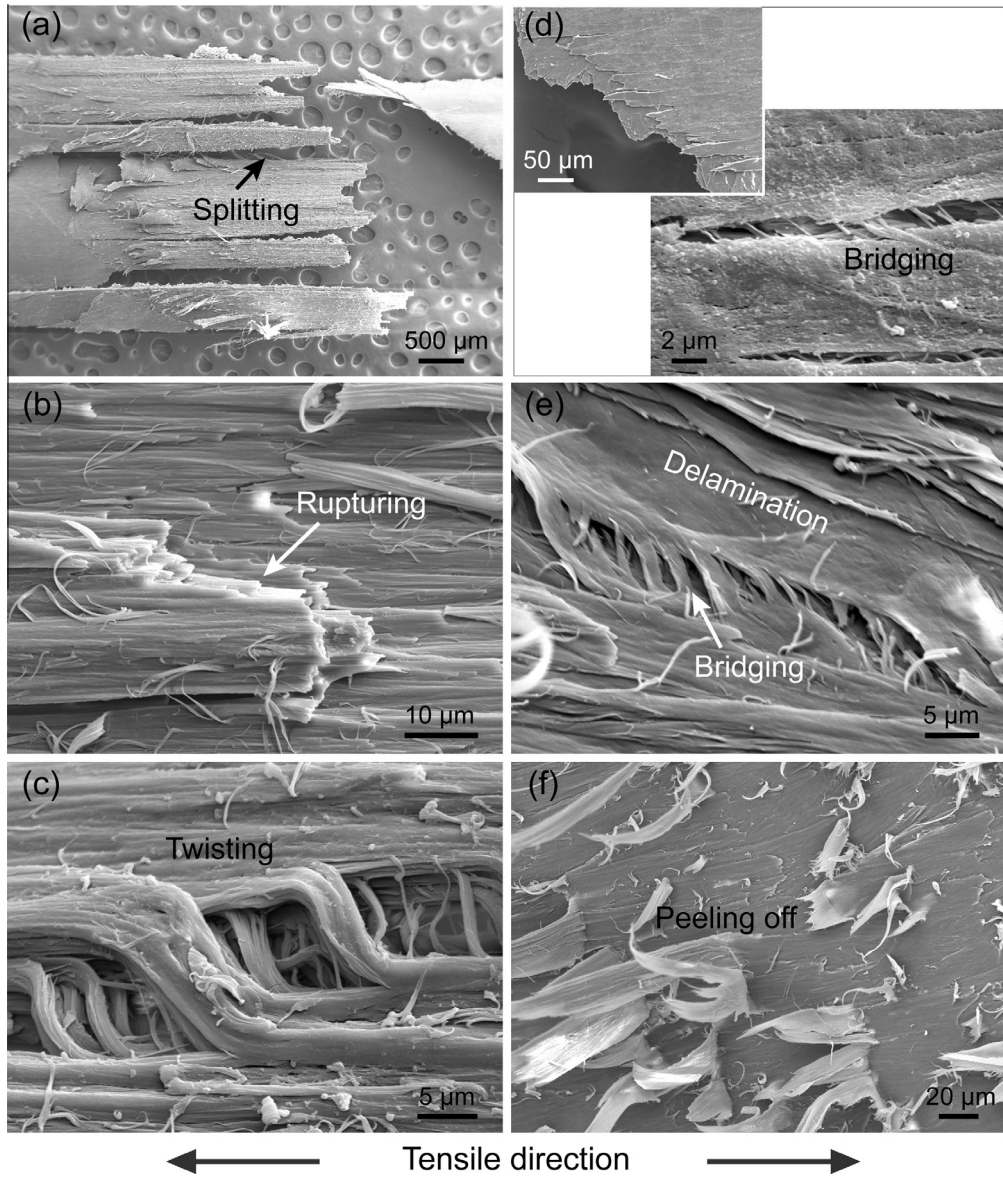


**Fig. 14.** SEM micrographs of tensile fractured dry cortex. Morphologies of (a–c) the detached substantia fibrosa and (d–f) the opposite side of cuticle.

pattern of horizontal grooves, as indicated by the dashed curves in Fig. 16(a). Cracks tend to initiate on the protrusion side at the buckled region and propagate toward opposite following a tortuous route in the direction perpendicular to loading axis (Fig. 16(b)). Through recovery, the shape of cells returns markedly to be almost equiaxed with the membranes sketched back (Fig. 16(c)). Nevertheless, both struts and membranes have been heavily deformed and damaged that cannot be fully recovered (Fig. 16(d)). The cell walls are split along struts within which the interior pores are ruptured. Meanwhile, a large number of wrinkled and torn regions are observed on the membranes, implying an evident mechanical contribution of membranes to the foam.

The deformation of closed-cell foam is mainly associated with three processes, i.e., cell edge bending, membrane stretching, and compression of inner gas [1]. In particular, the bending of cell edges causes cell faces or membranes to stretch in the direction perpendicular to compression. Meanwhile, the gas pressure increases with the volume reduction. Both the mechanisms, which are absent in open-cell foam, impose resistances to deformation and help to improve the stiffness. The relative Young's modulus

of foam with respect to that of corresponding solid can be expressed as [1]

$$\frac{E^F}{E^S} = \varphi^2 \left( \frac{\rho^F}{\rho^S} \right)^2 + (1 - \varphi) \frac{\rho^F}{\rho^S} + \frac{P_0(1 - 2v^F)}{E^S(1 - \rho^F/\rho^S)}, \quad (2)$$

where the three right terms describe the contributions from above three mechanisms.  $E$  and  $\rho$  denote Young's modulus and density, and the subscripts  $F$  and  $S$  indicate the foam and solid, respectively.  $v$  denotes Poisson's ratio of 0.3.  $P_0$  is the initial gas pressure which is expected to equal to the atmospheric pressure of  $\sim 0.1$  MPa. The parameter  $\varphi$  represents the volume fraction of solid contained in cell edges or struts. Because both foam and cortex are composed of  $\beta$ -keratin fibers, the properties of solid in foam have been approximated as those of cortex in this estimation without considering the effect of fiber arrangement. This assumption is also supported by experimental results that the hardness and Young's modulus vary slightly among different orientations in many fibrous biological materials [42–44]. By substituting experimental results,  $\varphi$  can be derived as  $\sim 0.94$  which conforms to the widespread distri-

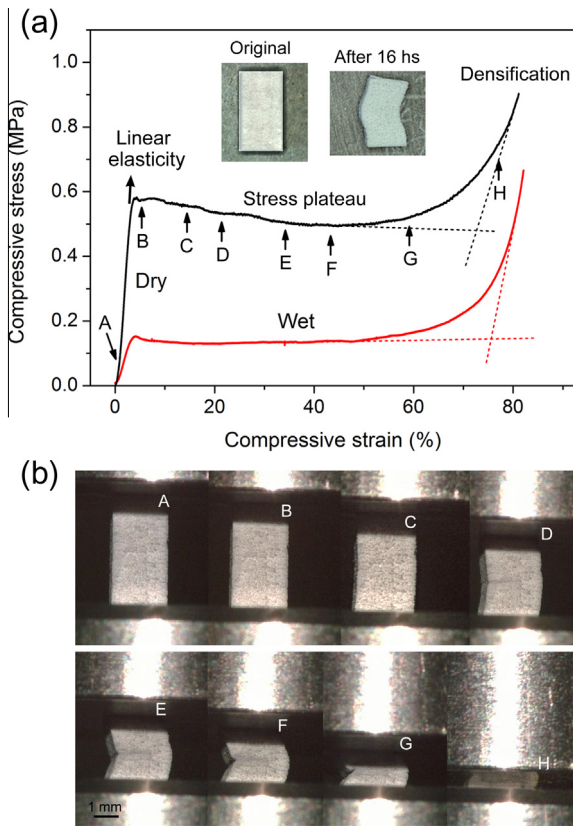


**Fig. 15.** (a) Representative compressive stress–strain curves of medullary foam under dry and wet conditions and (b) lateral appearances for the dry sample at different strains denoted by arrows. The recovery after unloading is illustrated in the inset in (a).

bution of thick struts within foam (Fig. 7). Accordingly, the membrane stretching plays a significant role in stiffening the foam by contributing about half to the global Young's modulus.

#### 4.3. Overall feather rachis

The mechanical properties have been further evaluated for overall feather rachis by compression under both dry and wet conditions. As shown in Fig. 17(a), the dry sample undergoes limited nominal plasticity and fails at  $\sim$ 13.8 MPa. Axial splitting and buckling occur on the shell of rachis (inset), which is analogous to the case of hollow cortex. Yet the splitting planes appear to be more plentiful and distributed more homogeneously around the circumference, implying that the stress state is more uniform at the ends. In comparison, the stress–strain curve of wet rachis exhibits a stress drop after initial linearity and then reaches a plateau followed by densification. The strength denoted as the critical stress for stress drop and Young's modulus are markedly lower than those of dry sample. The rachis deforms in the axisymmetric concertina buckling mode and no obvious splitting is observed on the shell (inset). This buckling mode is more uniform and tends to occur in thick, low modulus shells compared with the non-axisymmetric diamond buckling mode of the wet hollow cortex [39]. Thus the compressive stability of cortex is improved to a large extent by filling with foam.

In a general view, the properties of composites can be treated as weighted averages of those of their components [45]. In the present case, the cortex and foam undergo the same strain under compression. Thus the mechanical properties of overall rachis can be estimated according to the rule-of-mixtures under iso-strain condition by [45]

$$P^R = P^C V^C + P^F V^F \quad (3)$$

where  $P$  refers to the strength or Young's modulus, and  $V$  is the volume fraction of components. The subscripts  $C$  and  $F$  denote the cortex and foam, respectively. As illustrated in Fig. 17, both strength

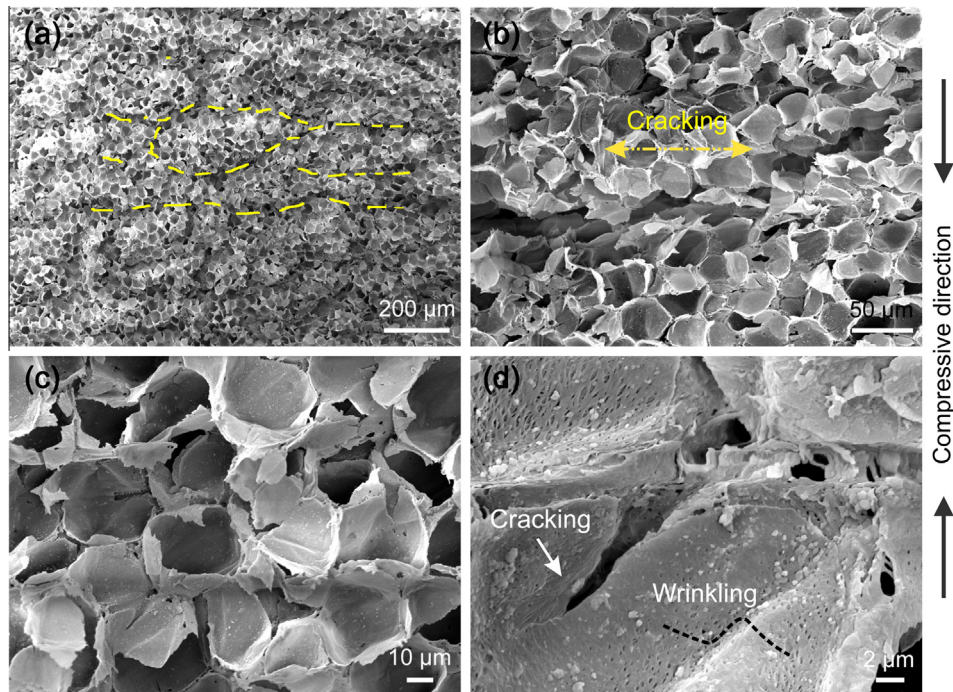


**Fig. 16.** SEM micrographs of partially recovered dry foam after compression.

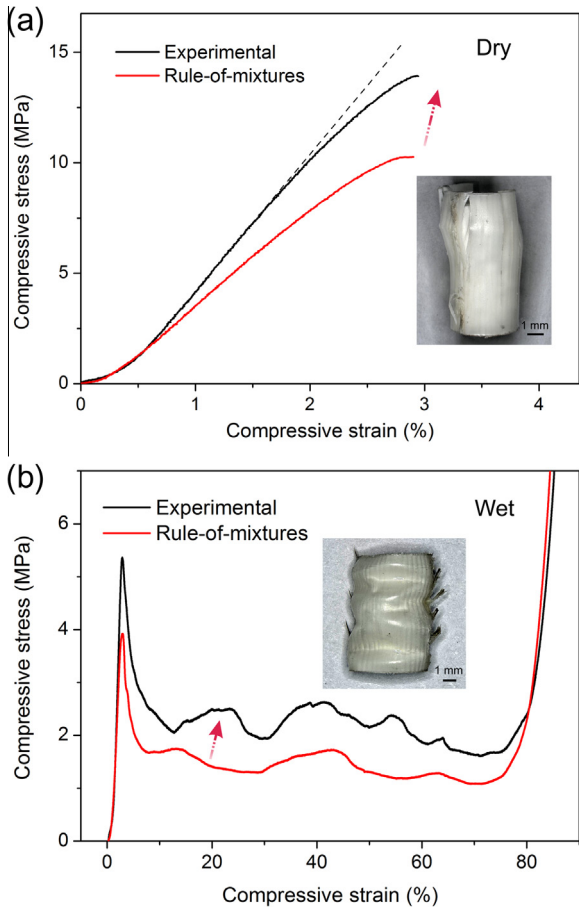


**Fig. 17.** Typical compressive stress–strain curves of overall feather rachis under (a) dry and (b) wet conditions along with the calculated ones according to the rule-of-mixtures. Macroscopic morphologies of failed samples are shown in insets.

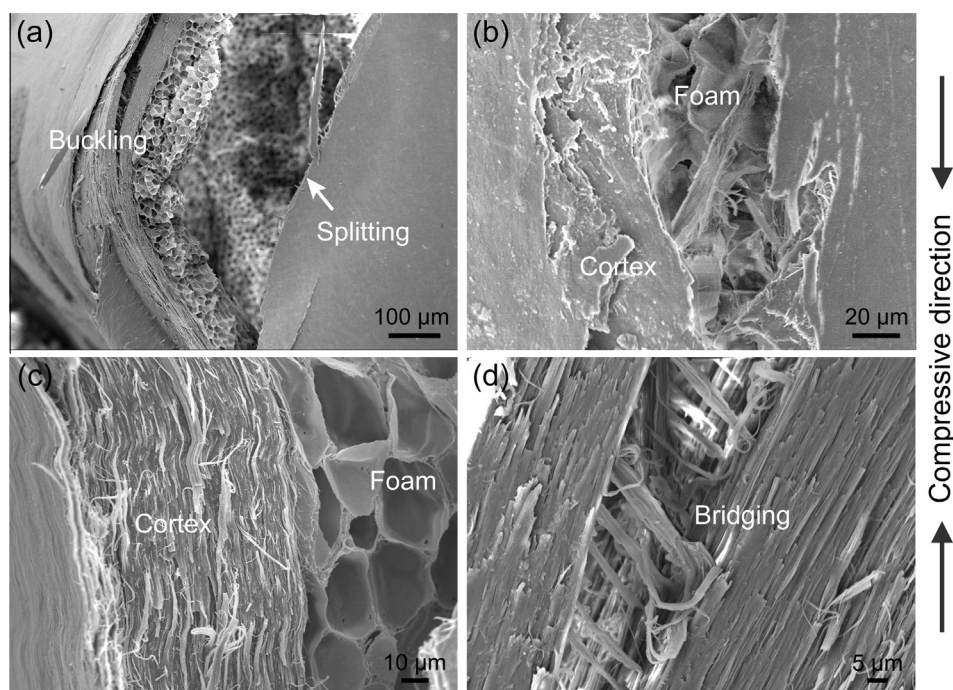
and Young's modulus are significantly improved compared with the deduced results under dry and wet conditions. Thus a synergetic effect is achieved in strengthening and stiffening the feather rachis.

Fig. 18 shows the morphologies of failed dry feather rachis. No obvious separation of cortex and foam occurs even after the severe buckling deformation, indicating a tight bonding between them. Both splitting and buckling of cortex are dragged by the interior foam and accompanied by its transverse stretching and rupture. The thickness of split pieces involved in buckling is further increased due to the attachment of a foam layer. Thus the mechanical properties can benefit from the tight interfacial bonding due to ridges and smooth transition, which is analogous to the case in porcupine quills [46]. Meanwhile, delamination appears more prominent in rachis compared with hollow cortex (Fig. 18(d)). As a consequence, interlamellar bridging effects on a greater number of cracking planes and plays a more significant role in toughening the rachis. In addition, local stress concentrations at the ends can be alleviated owing to the easy yielding and collapse of foam. The deformation of foam also helps to absorb certain amount of mechanical energy which otherwise would be used to promote failure. Besides, the gas pressure rising may contribute more in rachis compared with foam because the foam is further enveloped by outer cortex. Therefore, the presence of foam gives rise to higher failure resistance by retarding both splitting and buckling in comparison with hollow cortex. Strengthening, stiffening and toughening effects in both cortex and foam are also enhanced owing to their combinations. These endow the rachis more superior mechanical properties compared with the simple rule-of-mixtures interpolation.

Under axisymmetric buckling, the theoretical stress on the cortex shell of rachis can be obtained as follows [39]

$$\sigma_b^{CR} = \sqrt{3(1 - v^2)} \sigma_b^C, \quad (4)$$

where



**Fig. 18.** SEM micrographs of failed dry overall feather rachis after compression.

$$f = \frac{a/t}{12(1-v^2)(\lambda_{cr}/t)^2} + \frac{(\lambda_{cr}/t)^2}{a/t} + \frac{2aE^F}{Et(3-v^F)(1+v^F)} (\lambda_{cr}/t). \quad (5)$$

$\lambda_{cr}$  represents the critical buckling wavelength, and the subscripts CR and F denote the cortex and foam of rachis, respectively. For a first approximation,  $\lambda_{cr}/t$  can be accessed by considering the wrinkling of a flat sheet on an elastic foundation as below [39]

$$\lambda_{cr}/t = \left( \frac{(3-v^F)(1+v^F)}{12(1-v^2)} \right)^{1/3} (E/E^F)^{1/3}. \quad (6)$$

$\lambda_{cr}/t$  and  $f$  are calculated as 4.274 and 1.273, respectively. Accordingly, the critical stress sustained by cortex  $\sigma_b^{CR}$  can be deduced as ~287.1 MPa following Eq. (4). Then, the axial buckling strength of overall rachis can be obtained as ~32.5 MPa according to the following relation [39]

$$\sigma_b^R = 2t\sigma_b^{CR} \left( 1 + \frac{aE^F}{2tE} \right) / a, \quad (7)$$

which unreasonably exceeds the measured ultimate strength of ~13.8 MPa. Therefore, the strength of overall rachis is fundamentally controlled by axial splitting rather than buckling, which is analogous to the case of hollow cortex. It is suggested that the preference of splitting may be associated with the local stress constraint and concentration at the ends [38,46].

## 5. Potential implications for synthetic materials

Nature has long developed the ability to synthesize high-performance materials using simple constituent elements though various structural adaptations [3–9]. The elucidation of the structural features and their effects can enhance the understanding on naturally occurring strengthening, stiffening and toughening mechanisms, and provide inspiration for synthetic materials. For the present feather shaft, both the structure of its components and their combinations could contribute to improved mechanical properties. Firstly, the  $\beta$ -keratin fibers and fiber bundles are highly oriented along the length in substantia fibrosa to maximize its longitudinal stiffness. Meanwhile, the transverse separation of fibers can be hindered by the cuticula layer wherein the fibers intersect. Secondly, the robustness of foam benefits from the concentration of solid in struts, the stretching of thin membranes and the reinforcement of dense septa. An extremely low density can still be maintained owing to the high porosity and hierarchically cellular structure. Thirdly, the cortex is filled with foam in the feather rachis. The ridges and smooth transition give rise to a tight interfacial bonding between them. Both splitting and buckling are effectively retarded, contributing to a synergetic strengthening and stiffening effect. In addition, the macroscopic constituent and geometry, such as the proportions of components, sectional shape and area, are also adapted along the length to give sufficient bending stiffness and flexibility. Similar theorems may be utilized in the design of column and foam as well as their assembly in synthetic materials to optimize their properties from a bio-inspiration perspective. Moreover, the unraveled deformation and failure mechanisms in feather shaft and its components can also aid in understanding the mechanical behaviors of synthetic materials.

## 6. Conclusions

Based on the study of the structure and mechanical properties of peacock's tail coverts shaft and its components, the following conclusions can be obtained:

- (1) The feather shaft possesses a hierarchical structure at multiple length scales and varying constituent and geometry along its length. Both cortex and medullary foam are composed of  $\beta$ -keratin fibers in diameters of ~200–300 nm. The fibers are highly oriented longitudinally in substantia fibrosa and tilted by ~10–30° to form a staggered meshwork in cuticula of cortex. The equiaxed closed-cell foam manifests a low density and hierarchically cellular structure. Struts are interconnected to form a continuous skeleton and dense-packed septa serve as stiffeners. The interface between cortex and foam is featured by ridges and smooth transition which contribute to a tight adhesion. The minerals in feather shaft are identified as hydroxyapatite crystals and directly observed by TEM for the first time.
- (2) Both cortex and foam exhibit distinct mechanical behaviors under dry and wet conditions with lower strength and Young's modulus for wet samples. Axial splitting and subsequent buckling occur in dry cortex shell under compression. The compressive strength is deduced to be dominated by splitting, yet the tensile failure is dominated by rupture of fibers. Apparent delamination and intralamellar debonding occur and are bridged by abundant uncracked ligaments. In comparison, the compressive behavior of foam is featured by macroscopic buckling and three stages of linear elasticity, stress plateau and densification. Membrane stretching plays a significant role in stiffening the foam.
- (3) The overall feather rachis exhibit markedly higher strength and Young's modulus compared with the simple rule-of-mixtures interpolation, indicating a synergetic strengthening and stiffening effect. The failure resistance of dry cortex is effectively improved by filling with foam through retarding both splitting and buckling. The strength is dominated by axial splitting of cortex shell. The wet rachis deforms in the axisymmetric concertina buckling mode without obvious splitting, indicating improved compressive stability compared with hollow cortex. The unique mechanical properties, as well as deformation and failure behaviors and mechanisms, originating from the exquisite structural adaptations may have potential implications for synthetic materials.

## Acknowledgements

The authors are grateful to Dr. R.T. Qu and Dr. B. Wang for helpful discussion. This work was supported by the National Natural Science Foundation of China (Grant No. 51331007) and IMR SYNL-T.S. Kê Research Fellowship.

## Appendix A. Figures with essential color discrimination

Certain figures in this article, particularly Figs. 1–3, 5–8, 10–12 and 15–17, are difficult to interpret in black and white. The full color images can be found in the on-line version, at <http://dx.doi.org/10.1016/j.actbio.2015.01.035>.

## References

- [1] Gibson LJ, Ashby MF. Cellular solids: structure and properties. 2nd ed. Cambridge: Cambridge University Press; 1999.
- [2] Gibson LJ. Biomechanics of cellular solids. J Biomech 2005;38:377–99.
- [3] McKittrick J, Chen P-Y, Tombolato L, Novitskaya EE, Trim MW, Hirata GA, et al. Energy absorbent natural materials and bioinspired design strategies: a review. Mater Sci Eng C 2010;30:331–42.
- [4] Meyers MA, Chen P-Y, Lin AYM, Seki Y. Biological materials: structure and mechanical properties. Prog Mater Sci 2008;53:1–206.
- [5] Chen P-Y, McKittrick J, Meyers MA. Biological materials: functional adaptations and bioinspired designs. Prog Mater Sci 2012;57:1492–704.

- [6] Currey JD. *Bones: structure and mechanics*. Princeton: Princeton University Press; 2002.
- [7] Fratzl P, Weinkamer R. Nature's hierarchical materials. *Prog Mater Sci* 2007;52:1263–334.
- [8] Weinkamer R, Fratzl P. Mechanical adaptation of biological materials: the examples of bone and wood. *Mater Sci Eng C* 2011;31:1164–73.
- [9] Meyers MA, McKittrick J, Chen P-Y. Structural biological materials: critical mechanics-materials connections. *Science* 2013;339:773–9.
- [10] Seki Y, Bodde SG, Meyers MA. Toucan and hornbill beaks: a comparative study. *Acta Biomater* 2010;6:331–43.
- [11] Fratzl P. Biomimetic materials research: what can we really learn from nature's structural materials? *J R Soc Interface* 2007;4:637–42.
- [12] Hutmacher DW. Scaffolds in tissue engineering bone and cartilage. *Biomaterials* 2000;21:2529–43.
- [13] Freyman TM, Yannas IV, Gibson Lj. Cellular materials as porous scaffolds for tissue engineering. *Prog Mater Sci* 2001;46:273–82.
- [14] Lingham-Soliar T, Bonser RHC, Wesley-Smith J. Selective biodegradation of keratin matrix in feather rachis reveals classic bioengineering. *Proc Biol Sci* 2010;277:1161–8.
- [15] Bodde SG, Meyers MA, McKittrick J. Correlation of the mechanical and structural properties of cortical rachis keratin of retrices of the Toco Toucan (*Ramphastos toco*). *J Mech Behav Biomed Mater* 2011;4:723–32.
- [16] Wegst UGK, Ashby MF. The mechanical efficiency of natural materials. *Philos Mag* 2004;84:2167–81.
- [17] Petrie M, Tim H, Carolyn S. Peahens prefer peacocks with elaborate trains. *Anim Behav* 1991;41:323–31.
- [18] Filshie BK, Rogers GE. An electron microscope study of the fine structure of feather keratin. *J Cell Biol* 1962;13:1–12.
- [19] Fraser RDB, MacRae TP, Parry DAD, Suzuki E. The structure of feather keratin. *Polymer* 1971;12:35–56.
- [20] Fraser RDB, Parry DAD. Molecular packing in the feather keratin filament. *J Struct Biol* 2008;162:1–13.
- [21] Pabisch S, Puchegger S, Kirchner HOK, Weiss IM, Peterlik H. Keratin homogeneity in the tail feathers of *Pavo cristatus* and *Pavo cristatus* mut. alba. *J Struct Biol* 2010;172:270–5.
- [22] Purslow PP, Vincent JFV. Mechanical properties of primary feathers from the pigeon. *J Exp Biol* 1978;72:251–60.
- [23] Macleod GD. Mechanical properties of contour feathers. *J Exp Biol* 1980;87:65–71.
- [24] Bonser RHC, Purslow PP. The Young's modulus of feather keratin. *J Exp Biol* 1995;198:1029–33.
- [25] Bonser RHC. The mechanical properties of feather keratin. *J Zool* 1996;239:477–84.
- [26] Bonser RHC. The mechanical performance of medullary foam from feathers. *J Mater Sci Lett* 2001;20:941–2.
- [27] Cameron GJ, Wess TJ, Bonser RHC. Young's modulus varies with differential orientation of keratin in feathers. *J Struct Biol* 2003;143:118–23.
- [28] Weiss IM, Kirchner HOK. The peacock's train (*Pavo cristatus* and *Pavo cristatus* mut. alba) I. structure, mechanics, and chemistry of the tail feather covers. *J Exp Zool* 2010;313A:690–703.
- [29] Weiss IM, Schmitt KP, Kirchner HOK. The peacock's train (*Pavo cristatus* and *Pavo cristatus* mut. alba) II. the molecular parameters of feather keratin plasticity. *J Exp Zool* 2011;315:266–73.
- [30] McKittrick J, Chen P-Y, Bodde SG, Yang W, Novitskaya EE, Meyers MA. The structure, functions, and mechanical properties of keratin. *JOM* 2012;64:449–68.
- [31] Chen P-Y, Stokes AG, McKittrick J. Comparison of the structure and mechanical properties of bovine femur bone and antler of the North American elk (*Cervus elaphus canadensis*). *Acta Biomater* 2009;5:693–706.
- [32] Prum RO, Williamson S. Theory of the growth and evolution of feather shape. *J Exp Zool* 2001;291:30–57.
- [33] Bachmann T, Emmerlich J, Baumgartner W, Schneider JM, Wagner H. Flexural stiffness of feather shafts: geometry rules over material properties. *J Exp Biol* 2012;215:405–15.
- [34] Zhang Y, Yao H, Ortiz C, Xu J, Dao M. Bio-inspired interfacial strengthening strategy through geometrically interlocking designs. *J Mech Behav Biomed Mater* 2012;15:70–7.
- [35] Landis WJ, Glimcher MJ. Electron diffraction and electron probe microanalysis of the mineral phase of bone tissue prepared by anhydrous techniques. *J Ultrastruc Res* 1978;63:188–223.
- [36] Driessens FCM, Verbeeck RMH. *Biominerals*. Boca Raton: CRC Press; 1990.
- [37] Weiss IM, Kirchner HOK. Plasticity of two structural proteins: alpha-collagen and beta-keratin. *J Mech Behav Biomed Mater* 2011;4:733–43.
- [38] Timoshenko SP, Gere JM. *Theory of elastic stability*. 2nd ed. New York: McGraw-Hill; 1961.
- [39] Karam GN, Gibson Lj. Elastic buckling of cylindrical shells with elastic cores-I. analysis. *Int J Solids Struct* 1995;32:1259–83.
- [40] Takahashi K, Yamamoto H, Yokote Y, Hattori M. Thermal behavior of fowl feather keratin. *Biosci Biotech Biochem* 2004;68:1875–81.
- [41] Martin PA, Bradford GD, Gous RM. A formal method of determining the dietary amino acid requirements of laying-type pullets during their growing period. *Br Poult Sci* 1994;35:709–24.
- [42] Yang W, Gludovatz B, Zimmermann EA, Bale HA, Ritchie RO, Meyers MA. Structure and fracture resistance of alligator gar (*Atractosteus spatula*) armored fish scales. *Acta Biomater* 2013;9:5876–89.
- [43] Lin YS, Wei CT, Olevsky EA, Meyers MA. Mechanical properties and the laminate structure of *Arapaima gigas* scales. *J Mech Behav Biomed Mater* 2011;4:1145–56.
- [44] Wang R, Weiner S. Human root dentin: structural anisotropic and Vickers microhardness isotropy. *Connect Tissue Res* 1998;39:269–79.
- [45] Courtney TH. *Mechanical behavior of materials*. Beijing: China Machine Press; 2004.
- [46] Yang W, McKittrick J. Separating the influence of the cortex and foam on the mechanical properties of porcupine quills. *Acta Biomater* 2013;9:9065–74.